

1 **Measurements of Forbush decrease events at the center**
2 **of the South Atlantic Magnetic Anomaly with Muon**
3 **detectors**

4 **Jorge Molina^{1,2}, Euan Richard¹, Giovanni Secchia¹, Diego Stalder¹, Matias**
5 **Bertoli¹, Caleb Trepowski¹, Oscar Baez¹, Carlos Benitez Montiel³, Lucas**
6 **Cho¹, Esteban Cristaldo⁴, Pio Barrios¹, Jesus Nunez⁵ and Alan Cuevas¹**

7 ¹Facultad de Ingeniería, Universidad Nacional de Asunción, Campus de la UNA, San Lorenzo, Paraguay

8 ²Autoridad Reguladora Radiológica y Nuclear-ARRN, Campus de la UNA, San Lorenzo, Paraguay

9 ³Instituto de Física Corpuscular (IFIC), CSIC Universitat de València, Calle Catedrático José Beltrán, 2,

10 46980 Paterna, Valencia

11 ⁴Istituto Nazionale di Fisica Nucleare, Sezione di Milano Bicocca, I-20126, Milano

12 ⁵National Institute for Space Research - INPE, São José dos Campos, SP

13 **Key Points:**

- 14 • Commissioning of a compact muon detector in Paraguay.
15 • Correlation with Forbush decrease using Truncated Time Shift statistical test.

Corresponding author: Jorge Andres Molina, jmolina@ing.una.py

16 **Abstract**

17 A low cost muon detector was constructed in Paraguay, at the center of the South
 18 Atlantic Magnetic Anomaly (SAMA), where the Geomagnetic Cutoff Rigidity is 9.63 GV.
 19 The detector is of standard construction, with plates of scintillation material coupled to
 20 silicon photomultiplier (SiPM) sensors. To validate the system, we measured the aver-
 21 age muon flux rate and demonstrated its correlation with the disturbance storm time
 22 (Dst) geomagnetic index during the May and October 2024 Forbush decrease events. We
 23 use a recent statistical method to analyze the time series data, called the Truncated Time-
 24 Shift (TTS) test.

25 **Plain Language Summary**

26 The Earth's magnetic field protects humans and technology from radiation com-
 27 ing from outer space. However, it can be affected by "space weather" events such as so-
 28 lar flares. The field also has a weak spot above central South America, and satellites have
 29 been damaged while moving through this region. We constructed a particle detector at
 30 ground level in Paraguay, at the center of this weak spot. It can monitor several types
 31 of particles, including muons and gamma rays.

32 We measured the arrival rate of muons, and compared it to the magnetic field and
 33 neutron radiation measured by other detectors on the Earth's surface. At the times when
 34 the other detectors identified space weather events, we also saw a drop in the muon rate
 35 at our detector. This showed that our new detector can contribute to the detection and
 36 monitoring of space weather events, and effects due to the weak spot in the magnetic field.

37 **1 Introduction**

38 Cosmic Rays (CR) colliding with the Earth's atmosphere generate showers of sec-
 39 ondary particles, some of which reach the surface, where they are widely monitored and
 40 may be used to observe and predict space weather conditions. When disturbances in the
 41 Interplanetary Magnetic Field (IMF) caused by solar activity sweep over the planet, they
 42 may shield and reduce the arriving CR flux, causing a decline in the counting rate at the
 43 surface level. Particularly strong reductions in count rates (of at least several percent)
 44 are referred to as Forbush decreases (Kilifarska et al., 2020), which have been studied
 45 for more than 85 years (Cane, 2000), and can potentially be used in the forecasting of
 46 geomagnetic storms (Papailiou et al., 2024).

47 The flux of particles reaching the ground is being monitored by many detectors of
 48 various technologies and sizes around the world, at various geomagnetic cutoff rigidities,
 49 with some linked to global networks such as the Global Muon Detector Network (GMDN)
 50 (Rockenbach et al., n.d.) and the Neutron Monitor Database (NMDB) (Klein et al., 2010).

51 **1.1 The South Atlantic Magnetic Anomaly**

52 Detectors are particularly valuable in the SAMA, a region of low magnetic rigid-
 53 ity (Pavón-Carrasco & De Santis, 2016), where low-energy protons and electrons from
 54 the solar wind and cosmic rays penetrate to lower altitudes, rather than being contained
 55 within the Van Allen belts at higher altitudes. These particles are known to directly im-
 56 pact and damage satellites (Finlay et al., 2020) and upon reaching the ionosphere they
 57 can cause further particle showers, damaging the ozone layer (Pinto et al., 1990) and po-
 58 tentially increasing radiation at the ground level.

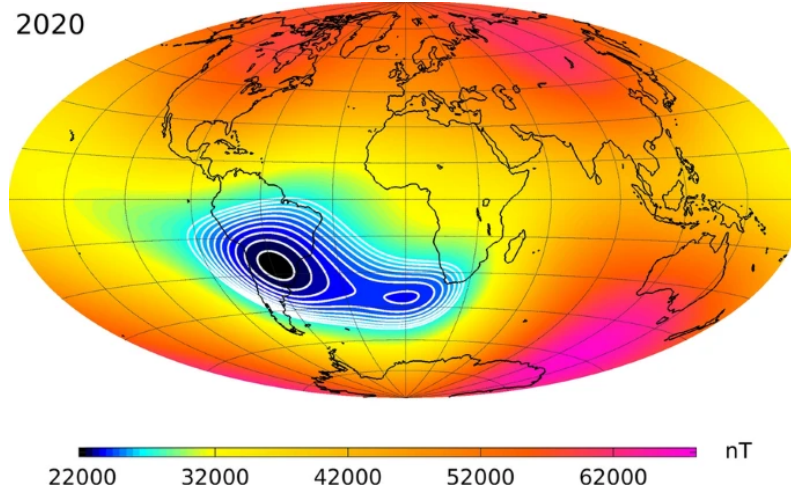


Figure 1: Magnetic field intensity at Earth’s Surface at year 2020, as estimated by the CHAOS-7 model (Finlay et al., 2020) based on data from the ESA’s Swarm (Friis-Christensen et al., 2006) satellites.¹

Fig. 1 shows that Paraguay is near the center of the SAMA, where the magnetic field currently has only half the strength expected from the dipole model. Measuring the muon flux here, and thus the geomagnetic conditions in the region, is particularly important due to the above-mentioned effects, and can help us further understand the behaviour of particle showers in this region.

Other muon flux measurements were performed close to the anomaly (Schuch, 2013), (Augusto et al., 2010), studying various aspects such as the day/night asymmetry, the Time of Flight (TOF), and the influence of atmospheric conditions on the arriving flux.

1.2 The FIUNA Muon Detector

In this work we will demonstrate that a relatively small and economical detector can measure the muon flux with sufficient sensitivity to detect space weather events. Our detector is stationed in the campus of the Facultad de Ingeniería de la Universidad Nacional de Asunción (FIUNA) with coordinates -25.330°N -57.519°W at an altitude of 132 m.

¹ Reproduced from (Finlay et al., 2020) under license CC BY 4.0 (<https://creativecommons.org/licenses/by/4.0/>).

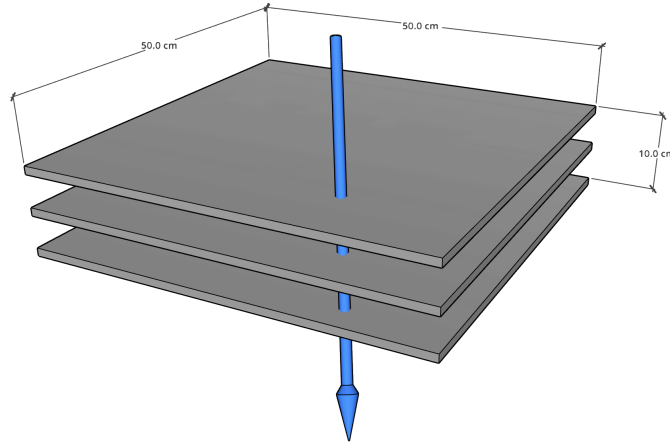


Figure 2: A simplified schematic view of the muon detector, showing the three-plate structure, with example muon track activating all three plates in coincidence.

In Sec. 2 we present further details of the detector and electronics; in Sec. 3 discuss data preparation and quality checks on the obtained data; in Sec. 4 analyse the muon flux, and compare it with geomagnetic activity over time using a novel statistical technique; and in Sec. 5 summarise and suggest future works.

2 Detection System

2.1 Physical Construction

The muon detector, as described in more detail in (Bertoli et al., 2023), consists of three 50×50 cm plastic scintillators, stacked above each other at 5 cm intervals as shown in Fig. 2, with each plate connected to four SiPMs by a bezel on each corner. Each SiPM is independently connected to a conditioning board, then to an FPGA board connected to a computer for data acquisition (DAQ).

The scintillator material is Eljen EJ-200 (Eljen Technology, Retrieved 2024-09-26), the SiPMs are Hamamatsu S13360-6050VE (“MPPC (Multi-Pixel Photon Counter) S13360-2050VE/-3050VE/-6050VE”, 2024), which have a breakdown voltage of 53 ± 5 V and a temperature coefficient of 54 mV/°C, and the FPGA board is a Digilent Basys 3 (Digilent, Retrieved 2024-09-26).

2.2 Signal Processing

The inverse polarization voltage of every SiPM is controlled with a precise voltage source, and is set to 53.5 V, which results in the SiPMs emitting a clear current pulse after the detection of incident photons. Each group of SiPM outputs (four per scintillation plate) is connected to a transimpedance amplifier on the conditioning board, summing the current pulses to produce three usable voltage channels, similar to typical implementations described in (Benitez Montiel et al., 2019). This signal then goes through an amplifier to a hysteresis comparator, which has a threshold value calibrated per channel to obtain maximum detection efficiency without introducing excess noise events, and provides a lengthened signal which is readable by the FPGA board.

98 **2.3 Data Acquisition**

99 The FPGA board receives the amplified and lengthened signal pulses, and a rising
100 edge detector triggers and sends the data through the internal logic design, which
101 was made with VIVADO (AMD, Retrieved 2024-11-27c) using a Microblaze microcon-
102 troller (AMD, Retrieved 2024-11-27a) programmed in C with VITIS (AMD, Retrieved
103 2024-11-27b). This design stores every trigger of a scintillator channel, either as a sin-
104 gle channel event, or as a simultaneous trigger of two or more incoming channels within
105 a 100 ns time window.

106 Each possible trigger combination is stored in separate 32-bit registers, which are
107 then sent through a multiplexer to the UART module of the FPGA board. This is con-
108 nected directly to a computer, which reads the data every second and stores it in an SQL
109 database every minute.

110 **3 Data Preparation**

111 **3.1 Dataset and Time Period**

112 As of May 6, 2024 the detector had reached a stable configuration and tuning, and
113 has since been in mostly continuous operation. The initial analysis in this paper was per-
114 formed using data from a fixed period up to June 24, 2024.

115 It is necessary to exclude periods of unstable operation within this timeframe. All
116 causes of such detector deadtime were concretely identified (such as DAQ computer er-
117 rors, faulty cables, test-runs or system restarts, and so on). Any hourly period with more
118 than 60 s of deadtime is discarded, and the remaining data is binned hourly; any period
119 with between 1 and 60 s of deadtime has its count rate rescaled based on the number of
120 operational seconds. The final hourly time-series data can be seen in Fig. 3, labeled “un-
121 corrected data”.

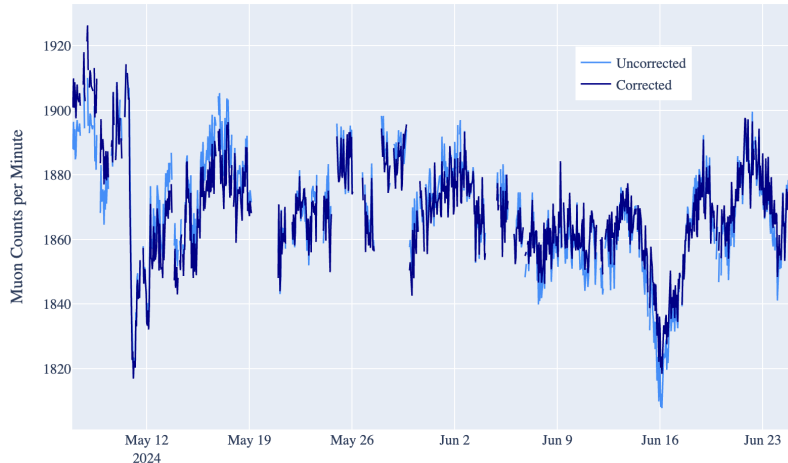


Figure 3: Muon counts per minute for the May–June analysis period, with deadtime removed. The counts adjusted for the SiPM temperature effect, plus atmospheric temper-
ature and pressure effects, are also shown.

122 **3.2 Temperature & Pressure Corrections**

123 ***3.2.1 Atmospheric Effects***

124 Before comparison with space weather phenomena, it is standard (Ri  digos et al.,
 125 2020) for ground-level detectors to correct for atmospheric temperature and pressure changes
 126 over time, as these affect particle shower propagation in the atmosphere. This allows a
 127 reconstruction of the primary CR flux arriving at the Earth, even though the detector
 128 is actually monitoring a secondary flux. A simple linear fit is usually sufficient to describe
 129 the relationship, expected to be on the order of $\sim 1\%$. We use temperature and pres-
 130 sure as recorded by external sensors on the FIUNA campus.

131 ***3.2.2 SiPM Temperature Dependence***

132 Separately and in addition to the atmospheric effects, it is known that the efficiency
 133 of SiPM detectors has an operating temperature dependence (Dinu, 2016). Despite a temperature-
 134 controlled environment within the laboratory, remaining temperature fluctuations (mon-
 135 itored by an additional internal sensor) mean that a $1 \sim 3\%$ variation in count rate is
 136 expected. Thus we apply an additional post-hoc correction to the detection rate to re-
 137 move this dependence.

138 ***3.2.3 Final Count-Rate Corrections***

139 Therefore, internal temperature, atmospheric temperature, and atmospheric pres-
 140 sure must be simultaneously corrected for. As these variables are expected to be strongly
 141 correlated, we apply a simultaneous multivariate linear fit of these variables against the
 142 count rate, on the entire dataset period binned per minute. The fitted parameters are
 143 given in Table 1. The values are roughly as expected, and when visualized describe the
 144 data well, therefore we consider this to be an accurate correction.

	Multivariate Linear Coefficient
Internal Temperature	-3.09 ± 0.71 counts $\text{min}^{-1} \text{ }^{\circ}\text{C}^{-1}$
Atmospheric Temperature	0.15 ± 0.04 counts $\text{min}^{-1} \text{ }^{\circ}\text{C}^{-1}$
Atmospheric Pressure	18.0 ± 21.5 counts $\text{min}^{-1} \text{ mBar}^{-1}$

Table 1: Fitted Temperature and Pressure Correction Coefficients

145 The final corrected muon counts over time are shown in Fig. 3.

146 **4 Measurements & Analysis**

147 **4.1 Muon Flux Measurement**

148 ***4.1.1 Incoming Flux and Detector Geometry***

149 Previous experiments around the globe (Borja et al., 2022) have shown that the
 150 muon flux arriving on the Earth's surface roughly follows the distribution

$$I(\theta) = I_0 \cos^2 \theta \quad (1)$$

151 where θ is the zenith angle from 0 (vertically above the detector) to $\pi/2$ (the horizon),
 152 and I_0 represents the vertical flux intensity in units of $\text{m}^{-2} \text{ s}^{-1} \text{ sr}^{-1}$. The quantity I_0 is
 153 commonly measured and compared between experiments; a standard value is often taken

154 to be $82 \text{ m}^{-2} \text{ s}^{-1} \text{ sr}^{-1}$ (Greisen, 1942), but measurements have been reported in the range
 155 from 62 to 128, depending on location and altitude (Borja et al., 2022).

156 The general expression for the number of particles entering a detector per second
 157 requires integrating the flux over solid angle Ω and the surface area of the detector S as

$$\int_{\Omega} \int_S I(\omega) (\mathbf{r} \cdot \mathbf{n}) d\omega dS \quad (2)$$

158 where \mathbf{r} is the unit vector to the solid angle $d\omega$, \mathbf{n} is the normal vector to the surface dS ,
 159 and it is assumed that $|\mathbf{r}| = 1$. This becomes easier to handle by switching to spherical
 160 coordinates (zenith θ , azimuth ϕ) for the incoming flux, and cartesian coordinates
 161 (x, y) for our detector's topmost surface, which is a simple 0.5 m wide square. The flux
 162 per second passing through all three scintillator plates on our detector may then be ex-
 163 pressed as

$$I_D = \int_{x=0}^{0.5} \int_{y=0}^{0.5} \int_{\theta=0}^{\pi/2} \int_{\phi=0}^{2\pi} I(\theta) \cos(\theta) \sin(\theta) A_B(\theta, \phi, x, y) d\phi d\theta dy dx \quad (3)$$

164 where $\cos(\theta)$ comes from the surface dot product, $\sin(\theta)$ from the Jacobian of the coor-
 165 dinate transformation, and A_B is the binary acceptance function of 0 or 1 — which ac-
 166 counts for the fact that an incoming particle striking the topmost surface may not pass
 167 through both lower plates, depending on its trajectory.

168 Assuming a flux $I(\theta)$ of the form in Eq. 1, and evaluating the integral, allows the
 169 simple representation

$$I_D = I_0 A \quad (4)$$

170 where A is an overall geometric factor known as the aperture of the detector, in units
 171 of $\text{m}^2 \text{ sr}$. We evaluated the integral according to an exact solution for this detector ge-
 172 ometry given in (Piazelli et al., 1976), and cross-checked with numerical integration of
 173 Eq. 3 using a geometric evaluation of the A_B term, with both calculations giving exactly
 174 $A = 0.3192 \text{ m}^2 \text{ sr}$.

175 4.1.2 Efficiency

176 The efficiency of the detection system ϵ , representing the fraction of real events cor-
 177 rectly observed by the detector, must also be evaluated. Firstly the efficiency of the mid-
 178 dle plate was estimated, by comparing the number of events that trigger only the top
 179 and bottom plates $T_{1,3}$ and events that trigger all three plates $T_{1,2,3}$, assuming that $T_{1,3}$
 180 represents true muon events passing through the detector without triggering the mid-
 181 dle plate. Further assuming that each of the three plates has a similar efficiency, the to-
 182 tal efficiency of our detector is given by

$$\epsilon = \left(\frac{T_{1,3}}{T_{1,2,3}} \right)^3 = 94.1\%. \quad (5)$$

183 Dark noise coincidence events and electronics related downtime are estimated to be neg-
 184 ligible.

185 4.1.3 Measured Flux

186 Considering Eqs. 4 and 5, the final expected count rate in s^{-1} would be given sim-
 187 plly by $I_0 A \epsilon$. Rearranging, we can express our own measured value of I_0 by

$$I_M = \frac{C}{A \epsilon T} \quad (6)$$

where C is the total sum of counts over the analysis period and T is the total detection time in seconds (where C was corrected for temperature effects and T for detector up-time as described in Sec. 3.2). Our measured average count rate is $C/T = 31.14\text{s}^{-1}$ and thus

$$I_M = 103.7 \text{ m}^{-2} \text{ s}^{-1} \text{ sr}^{-1} \quad (7)$$

with negligible statistical errors due to the long runtime.

This value is not unreasonable but is somewhat on the higher side when compared to existing measurements (Borja et al., 2022), which may be related to the specific location of our detector.

4.2 The Dst Index and Forbush Decreases

As already described, the muon flux at ground level varies over time according to many factors — such as atmospheric conditions, day-night asymmetry, and the strength of the magnetic field (Bektasoglu & Arslan, 2012). However as this is the first study with the muon detector, we intend to focus on a simple observation to confirm the correlation of the ground-level radiation with the strongest space weather effects. Therefore, we use the Dst index (Nose et al., 2015), which is a commonly-used if imperfect (Borovsky & Shprits, 2017) overall indicator of geomagnetic storm activity.

Luckily within the initial operating period of our detector, on May 10, 2024 a particularly strong Forbush decrease event was observed around the world. In Fig. 4 we see that this was clearly visible in both the Dst index, and in the nearest operational ground-level neutron monitor of the NMDB². The detection is seen two hours later in the latter, which is approximately the time delay expected (Baral et al., 2023; Badruddin et al., 2019).



Figure 4: Neutron counts from the Mexico station of the NMDB, plotted against the Dst index, for our analysis period.

4.2.1 Statistical Methodology

With the Forbush decrease occurring within our analysis period, we hope to see an obvious correlation between the muon rate at our detector and the Dst index. Nonethe-

² Mexico City neutron monitor data were kindly provided by the Cosmic Ray Group, Geophysical Institute, National Autonomous University of Mexico (UNAM), Mexico

less, before examining the data, we define a statistical significance test on the entire time range. It is a common technique in the field to compare the time-series by eye, select a time range, and apply a Pearson Correlation Coefficient; however such methods lead to over-fitting, and linear correlations have long been known to give incorrect results on time series (Yule, 1926) due to autocorrelation or other non-stationary behaviours (Rodríguez-Poo et al., 2014).

Thus, of the many options available, we choose the Truncated Time-Shift (TTS) test (Yuan & Shou, 2024); this generates alternative hypotheses by time-shifting one signal, but reweights the p -value to account for the similarity of shifted signals. Benefits of the TTS test are that it requires only one series to be stationary, and that compared to other commonly used tests it is particularly adept at rejecting false positives on various types of time series. The result is a u statistic which can be seen as an “upper limit” of the traditional p -value.

As this is a recent and lesser known test, to provide an example we first apply it to the Dst index & NMDB hourly data as was shown in Fig. 4, which are well-known to be strongly correlated. The Dst data passes an Augmented Dickey-Fuller (Dickey & Fuller, 1979) test with $p = 0.001$, which indicates enough stationarity that the TTS test should be applicable. The TTS r value is set at 50, and a time lag l of 2 hours is set (as is the expected physical delay as described in Section 4.2). Finally, as expected, a fairly strong correlation is seen with a TTS u -value of 0.059. We thus set our significance threshold as $u = 0.1$, in analogy to the common $p = 0.05$.

4.2.2 Results

We show the overlay of the corrected muon count rate & the Dst index in Fig. 5. The results of the TTS test on the full analysis period, with $r = 50$ and $l = 2$, indicate a correlation with a u -value of 0.020. As this paper was being prepared, a second Forbush decrease occurred on October 10, 2024. We thus added a second analysis period from September 16 to October 31, seen in Fig. 6, and applied an identical analysis procedure, which again indicated a correlation with $u = 0.078$.

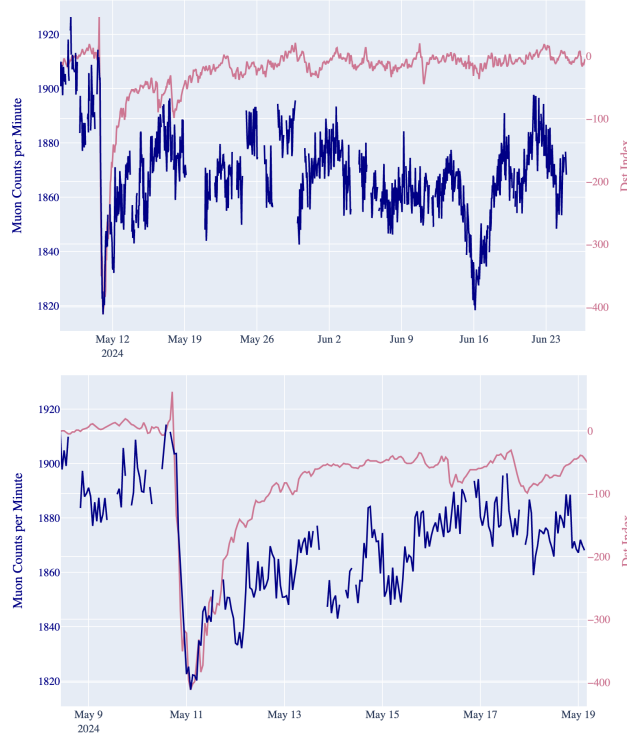


Figure 5: The corrected muon counts compared with the Dst Index, showing the full analysis period (upper) and zoomed in on the Forbush decrease and recovery period (lower).



Figure 6: As Fig. 5, but around the Forbush decrease of October 10, 2024.

Considering these results, an obvious correlation between the Dst decreases (caused by Forbush events) and a drop in muon detection rates in our detector can be seen, which is as expected. This gives us further confidence that our detector is accurately measuring the secondary CR muon flux.

There however do remain some other interesting features. For example, in Fig. 5, the muon rate does not seem to fully recover in the longer term, and there is a second large drop in counting rate on June 16th. Similarly in Fig. 6, a drop is seen on October 7th, before the primary Dst decrease. Unfortunately it is difficult to disentangle the physical implications of this, as the storm on this date caused an electrical blackout and a failure of the air conditioning units, which likely pushed the SiPM detectors beyond the ability of our linear temperature correction to perfectly compensate for.

5 Conclusion & Future Work

We have demonstrated the operation of a new muon detector at ground level inside the SAMA. Despite its relatively small size and low cost, the detector is able to successfully monitor the muon rate over time, as shown by its correlation with the Dst geomagnetic index, seen with TTS test significances of $u = 0.020$ and 0.078 on two separate analysis periods.

This initial commissioning result lays the foundation for ongoing observations and further enhancements to our suite of detectors.

It is clear that in this low-rigidity region, further studies to fully understand the interplay between space weather, ground observations, & geomagnetic effects would be useful – especially considering the practical impacts of the SAMA on satellites, electrical infrastructure, and the ozone layer.

Acknowledgments

The authors acknowledge the financial support given by the Engineering Faculty (FIUNA). Authors JM and DHS acknowledge the FEEI-PROCIENCIA-CONACYT-PRONII.

Open Research: Availability Statement

The datasets underpinning the study, *Forbush Decrease Events in the South Atlantic Magnetic Anomaly*, are openly accessible in the Zenodo repository (Molina et al., 2025). These datasets encompass time series of muon flux measurements, Disturbance Storm Time (Dst) index values, and neutron monitor data for both observation periods: May 2024 and October 2024.

The analysis code employed in this research, which includes the Jupyter Notebook detailing data processing and the implementation of the Truncated Time-Shift (TTS) test for time-series correlation analysis, is available in the GitHub repository: <https://github.com/diegostaPy/ForbushDecrease-SAMA->. This repository ensures transparency and reproducibility of the study's findings.

All datasets and software are licensed under the Creative Commons Attribution 4.0 International License (CC BY 4.0), permitting unrestricted use, distribution, and reproduction in any medium, provided the original work is properly cited.

281 **References**

- 282 AMD. (Retrieved 2024-11-27a). *Amd microblaze™ micro controller system (mcs)*.
 283 Website. Retrieved from [https://www.amd.com/en/products/software/adaptive-soecs-and-fpgas\(mb-mcs\).html](https://www.amd.com/en/products/software/adaptive-soecs-and-fpgas(mb-mcs).html)
- 284 AMD. (Retrieved 2024-11-27b). *Amd vitis™ unified software platform*. Website.
 285 Retrieved from <https://www.amd.com/en/products/software/adaptive-soecs-and-fpgas/vitis.html>
- 286 AMD. (Retrieved 2024-11-27c). *Amd vivado™ design suite*. Website. Retrieved from
 287 <https://www.amd.com/en/products/software/adaptive-soecs-and-fpgas/vivado.html>
- 288 Augusto, C., Navia, C., Tsui, K., Shigueoka, H., Miranda, P., Ticona, R., ... Saavedra, O. (2010). Simultaneous observation at sea level and at 5200 m.a.s.l. of high energy particles in the south atlantic anomaly. *Astroparticle Physics*, 34. doi: 10.1016/j.astropartphys.2010.04.005
- 289 Badruddin, B., Aslam, O. P. M., Derouich, M., Asiri, H., & Kudela, K. (2019).
 290 Forbush decreases and geomagnetic storms during a highly disturbed solar and
 291 interplanetary period, 4–10 september 2017. *Space Weather*, 17(3), 487-496. Retrieved from <https://agupubs.onlinelibrary.wiley.com/doi/abs/10.1029/2018SW001941> doi: <https://doi.org/10.1029/2018SW001941>
- 292 Baral, R., Adhikari, B., Calabia, A., Shah, M., Mishra, R. K., Silwal, A., ... Rodríguez Frías, M. D. (2023). Spectral features of forbush decreases during
 293 geomagnetic storms. *Journal of Atmospheric and Solar-Terrestrial Physics*, 242, 105981. Retrieved from <https://www.sciencedirect.com/science/article/pii/S1364682622001547> doi: <https://doi.org/10.1016/j.jastp.2022.105981>
- 294 Bektasoglu, M., & Arslan, H. (2012). Estimation of the effects of the earth's electric and magnetic fields on cosmic muons at sea level by geant4. *Journal of Atmospheric and Solar-Terrestrial Physics*, 74, 212-216. Retrieved from <https://www.sciencedirect.com/science/article/pii/S1364682611003063> doi: <https://doi.org/10.1016/j.jastp.2011.11.003>
- 295 Benítez Montiel, C., Aranda, D., Cristaldo, E., & Molina, J. (2019). Comparison between transimpedance and charge integrator amplification topologies for conditioning signals obtained from sipm sensors for the dune experiment. In *2019 ieee chilean conference on electrical, electronics engineering, information and communication technologies (chilecon)* (p. 1-5). doi: 10.1109/CHILECON47746.2019.8988108
- 296 Bertoli, M., Secchia, G., Molina Insfrán, J. A., Cristaldo Morales, E. J., Benítez Montiel, C. G., & Cuevas Mongelós, A. (2023). Optimization of a muon detection system with silicon photomultiplier sensors (sipm). In *2023 ieee chilean conference on electrical, electronics engineering, information and communication technologies (chilecon)* (p. 1-6). doi: 10.1109/CHILECON60335.2023.10418659
- 297 Borja, C., Ávila, C., Roque, G., & Sánchez, M. (2022). Atmospheric muon flux measurement near earth's equatorial line. *Instruments*, 6(4). Retrieved from <https://www.mdpi.com/2410-390X/6/4/78> doi: 10.3390/instruments6040078
- 298 Borovsky, J. E., & Shprits, Y. Y. (2017). Is the dst index sufficient to define all
 299 geospace storms? *Journal of Geophysical Research: Space Physics*, 122(11), 11,543-11,547. Retrieved from <https://agupubs.onlinelibrary.wiley.com/doi/abs/10.1002/2017JA024679> doi: <https://doi.org/10.1002/2017JA024679>
- 300 Cane, H. (2000, 1). Coronal mass ejections and forbush decreases. *Space Science Reviews*, 93. Retrieved from <https://www.osti.gov/biblio/4554034>
- 301 Dickey, D., & Fuller, W. (1979, 06). Distribution of the estimators for autoregressive time series with a unit root. *JASA. Journal of the American Statistical Association*, 74. doi: 10.2307/2286348
- 302 Digilent. (Retrieved 2024-09-26). *Basys 3 reference*. Website. Retrieved from

- 334 <https://digilent.com/reference/basys3/refmanual>
 335 Dinu, N. (2016). 8 - silicon photomultipliers (sipm). In B. Nabot (Ed.), *Photodetectors* (p. 255-294). Woodhead Publishing. Retrieved from <https://www.sciencedirect.com/science/article/pii/B9781782424451000087> doi:
 336 <https://doi.org/10.1016/B978-1-78242-445-1.00008-7>
 337 Eljen Technology. (Retrieved 2024-09-26). *General purpose ej-200, ej-204, ej-208, ej-212*. Website. Retrieved from <https://eljentechnology.com/products/plastic-scintillators/ej-200-ej-204-ej-208-ej-212>
 338 Finlay, C. C., Kloss, C., Olsen, N., Hammer, M. D., Tøffner-Clausen, L., Grayver,
 339 A., & Kuvshinov, A. (2020, Oct 20). The chaos-7 geomagnetic field model and
 340 observed changes in the south atlantic anomaly. *Earth, Planets and Space*, 72(1),
 341 156. Retrieved from <https://doi.org/10.1186/s40623-020-01252-9> doi:
 342 [10.1186/s40623-020-01252-9](https://doi.org/10.1186/s40623-020-01252-9)
 343 Friis-Christensen, E., Lühr, H., & Hulot, G. (2006, Apr 01). Swarm: A constellation
 344 to study the earth's magnetic field. *Earth, Planets and Space*, 58(4), 351-358. Re-
 345 tried from <https://doi.org/10.1186/BF03351933> doi: 10.1186/BF03351933
 346 Greisen, K. (1942, Mar). The intensities of the hard and soft components of cos-
 347 mic rays as functions of altitude and zenith angle. *Phys. Rev.*, 61, 212–221.
 348 Retrieved from <https://link.aps.org/doi/10.1103/PhysRev.61.212> doi:
 349 [10.1103/PhysRev.61.212](https://link.aps.org/doi/10.1103/PhysRev.61.212)
 350 Kilifarska, N. A., Bakmutov, V. G., & Melnyk, G. V. (2020). Chapter 5. galac-
 351 tic cosmic rays and solar particles in earth's atmosphere; section 5.1.1.2. short-
 352 term variations. In N. A. Kilifarska, V. G. Bakmutov, & G. V. Melnyk (Eds.),
 353 *The hidden link between earth's magnetic field and climate* (p. 101-131). Else-
 354 vier. Retrieved from <https://www.sciencedirect.com/science/article/pii/B978012819346400005X> doi: <https://doi.org/10.1016/B978-0-12-819346-4.00005-X>
 355 Klein, K.-L., Steigies, C., Steigies, C. T., Wimmer-Schweingruber, R. F., Kudela, K.,
 356 Ströharsky, I., ... García-Población, O. (2010, January). WWW.NMDB.EU: The
 357 real-time Neutron Monitor databas. In *38th cospar scientific assembly* (Vol. 38,
 358 p. 3).
 359 Molina, J., Richard, E., Giovanni, S., Stalder, D., Bertoli, M., Trepowski, C., ...
 360 Cuevas, A. (2025). *Measurements of forbush decrease events at the center of the*
 361 *south atlantic magnetic anomaly with muon detectors*. Zenodo. Retrieved from
 362 <https://doi.org/10.5281/zenodo.15032283> doi: 10.5281/zenodo.15032283
 363 Mppc (multi-pixel photon counter) s13360-2050ve/-3050ve/-6050ve [Computer
 364 software manual]. (2024). Retrieved from <https://www.hamamatsu.com/>
 365 [content/dam/hamamatsu-photonics/sites/documents/99_SALES_LIBRARY/ssd/s13360-2050ve_etc_kapd1053e.pdf](https://www.hamamatsu.com/dam/hamamatsu-photonics/sites/documents/99_SALES_LIBRARY/ssd/s13360-2050ve_etc_kapd1053e.pdf)
 366 Nose, M., Iyemori, T., Sugiura, M., & Kamei, T. (2015). *Geomagnetic dst index*.
 367 (World Data Center for Geomagnetism, Kyoto) doi: <https://doi.org/10.17593/14515-74000>
 368 Papailiou, M.-C., Abunina, M., Mavromichalaki, H., Shlyk, N., Belov, S., Abunin,
 369 A., ... Triantou, A. (2024). Precursory signs of large forbush decreases in relation
 370 to cosmic rays equatorial anisotropy variation. *Atmosphere*, 15(7). Retrieved from
 371 <https://www.mdpi.com/2073-4433/15/7/742> doi: 10.3390/atmos15070742
 372 Pavón-Carrasco, F. J., & De Santis, A. (2016). The south atlantic anomaly: The key
 373 for a possible geomagnetic reversal. *Frontiers in Earth Science*, 4. Retrieved from
 374 <https://www.frontiersin.org/journals/earth-science/articles/10.3389/feart.2016.00040> doi: 10.3389/feart.2016.00040
 375 Piazolli, B., Mannocchi, G., Melone, S., Picchi, P., & R., V. (1976, 1). Aperture and
 376 counting rate of rectangular telescopes for single and multiple parallel particles.
 377 *Nuclear Instruments and Methods*, 135.

- 387 Pinto, J., O., Kirchhoff, V. W. J. H., & Gonzalez, W. D. (1990, May). Mesospheric
388 ozone depletion due to energetic electron precipitation at the South Atlantic mag-
389 netic anomaly. *Annales Geophysicae*, 8, 365-367.
- 390 Riádigos, I., García-Castro, D., González-Díaz, D., & Pérez-Muñozuri, V. (2020).
391 Atmospheric temperature effect in secondary cosmic rays observed with a 2
392 square meter ground-based trpc detector. *Earth and Space Science*, 7(9),
393 e2020EA001131. Retrieved from <https://agupubs.onlinelibrary.wiley.com/doi/abs/10.1029/2020EA001131> (e2020EA001131 10.1029/2020EA001131) doi:
394 <https://doi.org/10.1029/2020EA001131>
- 395 Rockenbach, M., Dal Lago, A., Schuch, N. J., Munakata, K., Kuwabara, T., Oliveira,
396 A. G., ... Sabbah, I. (n.d.).
- 397 Rodríguez-Poo, J., Moral, I., Aparicio, T., Villanúa, I., Cizek, P., Xia, Y., ...
398 Čížková, L. (2014). *Computer-aided introduction to econometrics*. Springer
399 Science Business Media, 2012.
- 400 Schuch, N. J. (2013). The global muon detector network - gmdn the brazilian contribu-
401 tion for space weather forecasting. In *33rd international cosmic ray conference*
402 (p. 0946).
- 403 Yuan, A., & Shou, W. (2024, 08). A rigorous and versatile statistical test for cor-
404 relations between stationary time series. *PLOS Biology*, 22(8), 1-26. Retrieved
405 from <https://doi.org/10.1371/journal.pbio.3002758> doi: 10.1371/journal
406 .pbio.3002758
- 407 Yule, G. U. (1926). Why do we sometimes get nonsense-correlations be-
408 tween time-series?—a study in sampling and the nature of time-series. *Jour-*
409 *nal of the Royal Statistical Society*, 89(1), 1-63. Retrieved 2024-07-10, from
410 <http://www.jstor.org/stable/2341482>